remote sensing

MDPI

Article

Tectonic Activity Analysis of the Laji-Jishi Shan Fault Zone: Insights from Geomorphic Indices and Crustal Deformation Data

Yujie Ma [1], Weiliang Huang [1,*], Jiale Zhang [1], Yan Wang [1], Dong Yu [1] and Baotian Pan [2]

[1] College of Geological Engineering and Surveying of Chang'an University, Key Laboratory of Western China Mineral Resources and Geological Engineering, Xi'an 710054, China; 2022226084@chd.edu.cn (Y.M.); 2021126095@chd.edu.cn (J.Z.); 2022126111@chd.edu.cn (Y.W.); 2022226115@chd.edu.cn (D.Y.)
[2] College of Earth and Environmental Sciences, Lanzhou University, Lanzhou 730000, China; panbt@lzu.edu.cn
* Correspondence: huangweiliang@chd.edu.cn

Abstract: Fault segmentation plays a critical role in assessing seismic hazards, particularly in tectonically complex regions. The Laji-Jishi Shan Fault Zone (LJSFZ), located on the northeastern margin of the Tibetan Plateau, is a key structure that accommodates regional tectonic stress. This study integrates geomorphic indices, cross-fault deformation rate profiles, and 3D crustal electrical structure data to analyze the varying levels of tectonic activity across different segments of the LJSFZ. We extracted 160 drainage basins along the strike of the LJSFZ from a 30 m resolution digital elevation model and calculated geomorphic indices, including the hypsometric integral (*HI*), stream length-gradient index (*SL*), and channel steepness index (k_{sn}), to assess the variations in tectonic activity intensity along the strike of the LJSFZ. The basins were categorized based on river flow directions to capture potential differences across the fault zone. Our results show that the eastern basins of the LJSFZ exhibit the strongest tectonic activity, demonstrated by significantly higher *SL* and k_{sn} values compared to other regions. A detailed segmentation analysis along the northern Laji Shan Fault and eastern Jishi Shan Fault identified distinct fault segments characterized by variations in *SL* and k_{sn} indices. Segments with high *SL* values (>500) correspond to higher crustal uplift rates (~3 mm/year), while segments with lower *SL* values exhibit lower uplift rates (~2 mm/year), as confirmed by cross-fault deformation profiles derived from GNSS and InSAR data. This correlation demonstrates that geomorphic indices effectively reflect fault activity intensity. Additionally, 3D crustal electrical structure data further indicate that highly conductive mid- to lower-crustal materials originating from the interior of the Tibetan Plateau are obstructed at segment L3 of the LJSFZ. This obstruction leads to localized intense uplift and enhanced fault activity. These findings suggest that while the regional stress–strain pattern of the northeastern Tibetan Plateau is the primary driver of the segmented activity along the Laji-Jishi Shan belt, the direction of localized crustal flow is a critical factor influencing fault activity segmentation.

Keywords: tectonic activity; drainage analysis; geomorphic indices; Laji-Jishi Shan Fault Zone; seismic hazard

Citation: Ma, Y.; Huang, W.; Zhang, J.; Wang, Y.; Yu, D.; Pan, B. Tectonic Activity Analysis of the Laji-Jishi Shan Fault Zone: Insights from Geomorphic Indices and Crustal Deformation Data. *Remote Sens.* **2024**, *16*, 3770. https://doi.org/10.3390/rs16203770

Academic Editors: Zhongtai He, Wenliang Jiang, Dong Li and Erick Mas

Received: 15 August 2024
Revised: 8 October 2024
Accepted: 9 October 2024
Published: 11 October 2024

1. Introduction

A fundamental observation in seismology is that most major faults do not rupture along their entire length during an earthquake; instead, ruptures typically occur within one or a few segments, each characterized by a distinct rupture history [1–3]. The segmentation of fault rupture is controlled by variations in fault geometry, material properties, and tectonic activity across different segments [4–6]. Accurately identifying these fault segments is not only crucial for understanding fault mechanics [7] but also for estimating potential rupture lengths and predicting the maximum earthquake magnitude, thereby enhancing the accuracy of seismic risk assessments [4,5,8].

The Laji-Jishi Shan Fault Zone (LJSFZ, with 'Shan' meaning 'mountains' in Chinese), located on the northeastern margin of the Tibetan Plateau, is a key structure that accommodates the region's tectonic stress [9–11]. Understanding the segmentation of this fault zone is critical for assessing seismic hazards in the area. The significance of this fault zone was underscored by the magnitude 6.2 earthquake (Ms 6.2) that struck the LJSFZ at a depth of 10 km on 18 December 2023, resulting in 1130 casualties and the destruction of 15,000 buildings. This event highlights the urgent need to accurately evaluate the seismic potential of different segments within the LJSFZ. The fault zone, which consists of a series of parallel thrust faults that delineate the boundaries between the Laji Shan and Jishi Shan mountain ranges and the adjacent basins, extends approximately 220 km [10] (see Figure 1b). Its complex "S"-shaped geometry, with multiple pronounced bends—some approaching 40°—indicates significant segmentation [12,13], emphasizing the need for detailed fault segmentation analysis to accurately evaluate seismic potential.

Previous studies attempted to segment the LJSFZ based on the continuity and spatial distribution of surface traces [10,14,15]. However, the ambiguous nature of these surface traces often results in segmentation outcomes that heavily depend on subjective interpretation, leading to considerable uncertainty. Recent advances in geomorphic analysis, particularly using indices derived from remote sensing data, have provided new methods for identifying and characterizing fault segments [16–22]. Indices such as hypsometric integral (*HI*), stream length-gradient (*SL*), and valley floor width-to-height ratio (VF) have proven effective in identifying regions of enhanced tectonic deformation. However, existing studies typically reflect only relative tectonic activity levels and often lack detailed, reliable comparative evidence that integrates these indices with absolute crustal deformation rates [23–25]. Moreover, the role of deep crustal processes in influencing fault zone segmentation has not yet been fully explored [26–28], particularly in geologically complex regions like the LJSFZ. This limitation hinders our understanding of fault activity behavior and the distribution of strong earthquakes.

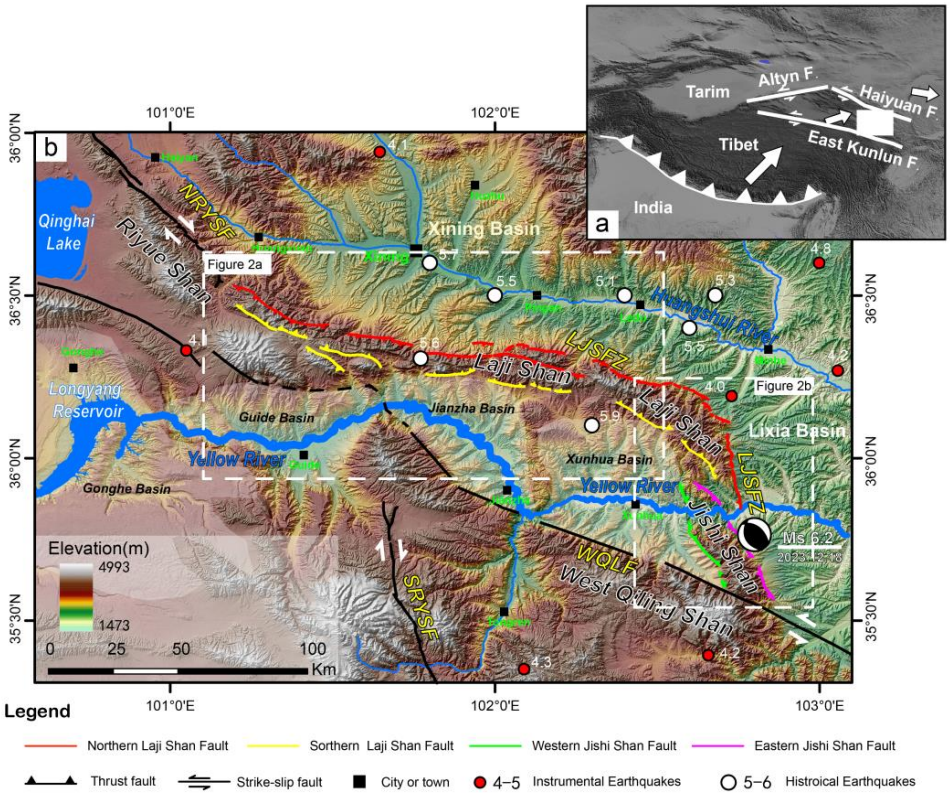

Figure 1. Tectonic background and topographic features of the LJSFZ, northeastern Tibetan Plateau. (**a**) Major tectonic structures across the Tibetan Plateau (modified from Huang (2019) [29]), with the

white square indicating the area shown in (**b**). (**b**) Color-shaded relief map compiled using active fault and earthquake information of the northeastern Tibetan Plateau. The active faults' data are from Chinese Seismic Intensity Zoning Map (GB18306-2015) [30] and Zhang (2012) [31]. Earthquake locations is from Cheng et al. (2017) [32]. Abbreviations: NRYSF: North Riyue Shan Fault; SRYSF: Sorth Riyue Shan Fault; WQLF: West Qinling Fault.

This study integrated geomorphic indices, cross-fault deformation rate profiles, and 3D crustal electrical structure data to analyze the tectonic activity of different segments within the LJSFZ. Our results showed that the eastern basins of the LJSFZ exhibit the strongest tectonic activity, with significant variations in the *SL* and k_{sn} indices along the fault's strike revealing distinct segmentation characteristics. These segmentation features are further clarified through comparisons with cross-fault deformation data. This study also examined the dynamic mechanisms behind spatial variability in fault activity, emphasizing the role of deep crustal flow. The direction of this localized crustal flow emerged as a key factor in fault segmentation, providing deeper insights into the LJSFZ's segmentation and kinematics.

2. Geological Background

The ongoing convergence between the Indian Plate and the Asian continent has uplifted the Tibetan Plateau (Figure 1a). The northeastern margin of the plateau, which is its youngest and most actively deforming part, has experienced significant surface uplift [33–35]. This uplift is attributed to the NE–SW oblique shortening, resulting from the northeastward propagation of the plateau. This process is accompanied by east–west left-lateral shearing along the East Kunlun and Haiyuan faults (Figure 1b), leading to the formation of a series of NW–SE trending linear arcuate mountain ranges and intervening basins [10,36] (Figure 1a). Among these mountain ranges, the Laji-Jishi Shan belts, which curve convexly to the northeast, are particularly prominent. The Laji Shan merges obliquely with the Riyue Shan fault to the northwest and continues to the short Jishi Shan to the southeast. The Laji and Jishi Shan belts are separate, aligned in a right-overstepping en echelon pattern (Figure 1b). The Jishi Shan ends against the West Qinling fault, which formed as an active left-lateral fault [37]. The Laji-Jishi Shan belt comprises four major active faults: the Northern Laji Shan, Southern Laji Shan, Eastern Jishi Shan, and Western Jishi Shan faults (Figure 1b). Among these, the Northern Laji Shan Fault and Eastern Jishi Shan Fault serve as the primary boundary faults of the Laji-Jishi Shan belt, playing a crucial role in the orogenesis [10,38].

The Laji-Jishi Shan belt has been uplifted by tectonic activity, exposing rocks with a long geologic history. These rocks include ultramafic and mafic magmatic rocks, abyssal sedimentary deposits from the early Paleozoic, and metamorphic rocks from the Proterozoic, forming a mélange [10]. The uplift of the Laji Shan began around 22 Ma years ago, as indicated by the doubling of sedimentation rates in nearby Cenozoic basins and the incorporation of freshly eroded detrital zircons into the sedimentary deposits, suggesting the emergence of Laji Shan as a topographic high and a new source area [11,39,40]. In contrast, the nearly north–south trending Jishi Shan experienced uplift later, between 8 and 13 Ma ago [41]. During this interval, the direction of crustal shortening in the northeastern Tibetan Plateau shifted from a north–south orientation to a northeast–southwest and, in some areas, even east–west [12].

Since the Quaternary, the Yellow River has incised through the Laji-Jishi Shan belt, continuing into the interior of the plateau. The river's incision reflects an uplift rate of 2–6 mm/year for the Laji-Jishi Shan belt, resulting in steep escarpments on either side [42]. Recent three-dimensional deformation maps obtained using GNSS and InSAR data revealed that the Jishi Shan continues to uplift at a rate of 3–4 mm/year [43].

The spatial distribution of earthquakes in this region exhibits notable heterogeneity, with a significant concentration of historical seismic events along the Huangshui River in the Xining Basin to the north (Figure 1b). This pattern largely reflects the limitations of historical records, which are influenced by population density and the locations of settlements rather than the underlying tectonic structures. In contrast, the 2023 Ms 6.2 earthquake is the largest recorded event on the LJSFZ. This significant event underscores the incomplete nature of historical records and emphasizes the importance of assessing the seismic potential of this fault zone.

3. Data and Methodology

This study utilized the 30 m resolution Copernicus Digital Elevation Model (COP-DEM) to analyze the drainage network of Laji Shan and Jishi Shan. The drainage network was extracted using RiverTools 3.0 and ArcGIS 9.2, extending from the drainage divides to the range-front faults. In areas where these faults are indistinct, drainage basin outlets were identified by sudden changes in terrain slope (Figure 2). The topographic profiles indicated that the piedmont slopes are generally less than 20°; so, a 20° slope threshold was used to define the mountain boundaries (Figure 2).

To assess the intensity of tectonic activity along the strike of LJSFZ, we selected a total of 160 drainage basins, ranging from 1.0 to 37.3 km^2, for detailed analysis. Basins with smaller areas or where the main river intersected the range-front faults at angles less than 40° were excluded. For each basin, we calculated the hypsometric integral (*HI*), stream length-gradient index (*SL*), and channel steepness index (k_{sn}). These indices were derived using RiverTools 3.0, ArcGIS 9.2 and MATLAB R2024a to ensure accurate extraction and computation across the selected basins [20,44,45] (Tables 1–4).

Table 1. The *SL* and k_{sn} values of the streams, along with the *HI* values of the drainage basins, in the northern section.

ID	*HI*	*SL*	k_{sn}	ID	*HI*	*SL*	k_{sn}	ID	*HI*	*SL*	k_{sn}	ID	*HI*	*SL*	k_{sn}
1	0.45	213	87	18	0.47	237	107	35	0.41	222	93	52	0.44	473	158
2	0.50	315	127	19	0.44	204	92	36	0.42	210	87	53	0.50	471	143
3	0.52	279	118	20	0.47	218	92	37	0.37	201	65	54	0.52	306	143
4	0.49	376	135	21	0.49	274	116	38	0.50	157	86	55	0.50	266	119
5	0.55	510	150	22	0.48	408	133	39	0.43	128	60	56	0.44	321	116
6	0.50	412	114	23	0.43	319	100	40	0.38	174	64	57	0.40	432	123
7	0.53	368	124	24	0.51	188	74	41	0.48	214	84	58	0.50	516	154
8	0.48	309	113	25	0.45	208	78	42	0.51	261	88	59	0.52	655	177
9	0.41	321	89	26	0.51	194	77	43	0.55	197	74	60	0.57	705	168
10	0.41	243	94	27	0.37	278	95	44	0.47	185	70	61	0.62	714	162
11	0.40	196	87	28	0.36	281	84	45	0.43	162	65	62	0.58	402	131
12	0.42	181	85	29	0.46	290	122	46	0.53	182	73	63	0.59	798	191
13	0.45	238	77	30	0.46	338	145	47	0.46	312	106	64	0.56	703	161
14	0.53	346	81	31	0.49	326	121	48	0.49	244	92	65	0.54	666	174
15	0.49	151	76	32	0.48	244	117	49	0.46	189	52	66	0.49	557	161
16	0.51	237	97	33	0.58	293	122	50	0.53	176	76	67	0.50	371	121
17	0.41	205	63	34	0.51	293	120	51	0.50	353	111				

Table 2. The *SL* and k_{sn} values of the streams, along with the *HI* values of the drainage basins, in the eastern section.

ID	*HI*	*SL*	k_{sn}	ID	*HI*	*SL*	k_{sn}	ID	*HI*	*SL*	k_{sn}	ID	*HI*	*SL*	k_{sn}
68	0.48	364	138	76	0.52	405	133	84	0.53	683	110	92	0.53	870	180
69	0.46	449	131	77	0.48	482	127	85	0.50	524	107	93	0.63	447	154
70	0.46	500	102	78	0.43	479	115	86	0.50	783	194	94	0.48	380	156
71	0.46	593	102	79	0.61	398	161	87	0.64	819	190	95	0.35	711	167
72	0.49	427	128	80	0.48	195	89	88	0.46	1253	142	96	0.51	550	170
73	0.51	804	159	81	0.50	274	113	89	0.48	979	169	97	0.47	475	147
74	0.49	531	104	82	0.66	530	147	90	0.54	643	173				
75	0.51	512	122	83	0.48	821	118	91	0.51	794	132				

Table 3. The *SL* and k_{sn} values of the streams, along with the *HI* values of the drainage basins, in the southern section.

ID	*HI*	*SL*	k_{sn}	ID	*HI*	*SL*	k_{sn}	ID	*HI*	*SL*	k_{sn}	ID	*HI*	*SL*	k_{sn}
98	0.43	218	64	109	0.42	200	54	120	0.56	425	88	131	0.49	143	82
99	0.49	170	71	110	0.45	170	73	121	0.52	229	81	132	0.66	270	129
100	0.49	226	69	111	0.43	798	144	122	0.49	162	83	133	0.42	324	99
101	0.49	185	89	112	0.54	392	165	123	0.54	290	92	134	0.42	294	103
102	0.48	346	114	113	0.50	526	137	124	0.51	172	73	135	0.43	375	87
103	0.52	424	134	114	0.55	329	105	125	0.54	395	132	136	0.46	294	103
104	0.55	413	127	115	0.43	192	79	126	0.54	382	115	137	0.44	280	99
105	0.58	606	259	116	0.47	136	66	127	0.53	264	93	138	0.53	498	135
106	0.50	386	111	117	0.53	290	100	128	0.43	180	72				
107	0.48	209	98	118	0.52	320	102	129	0.56	236	137				
108	0.46	218	94	119	0.46	307	91	130	0.47	158	82				

Table 4. The *SL* and k_{sn} values of the streams, along with the *HI* values of the drainage basins, in the western section.

ID	*HI*	*SL*	k_{sn}	ID	*HI*	*SL*	k_{sn}	ID	*HI*	*SL*	k_{sn}	ID	*HI*	*SL*	k_{sn}
139	0.58	381	123	145	0.51	243	61	151	0.56	687	132	157	0.53	336	127
140	0.54	337	108	146	0.45	255	94	152	0.57	815	116	158	0.47	705	188
141	0.50	253	88	147	0.45	138	58	153	0.51	657	143	159	0.43	473	144
142	0.49	268	94	148	0.39	423	69	154	0.45	688	132	160	0.51	405	121
143	0.50	283	101	149	0.48	460	76	155	0.60	546	78				
144	0.48	346	72	150	0.53	494	126	156	0.46	694	168				

Given the complex geometry of the Laji-Jishi Shan belt, which likely reflects differential tectonic uplift in various directions, we divided the drainage basins into four regions based on the flow direction of their rivers: southern, northern, eastern, and western. This division aligns with the natural flow directions of the rivers and is intended to capture potential differences in geomorphic responses that may be associated with varying tectonic activities across the different segments of the Laji-Jishi Shan belt.

Our methodology involved first comparing the geomorphic indices (*HI*, *SL*, k_{sn}) across these four directional categories to highlight the variability in tectonic activity. Following this regional analysis, we conducted a detailed segmentation study focusing on the Northern Laji Shan Fault and Eastern Jishi Shan Fault, which involved a closer examination of the tectonic segmentation characteristics within these specific areas.

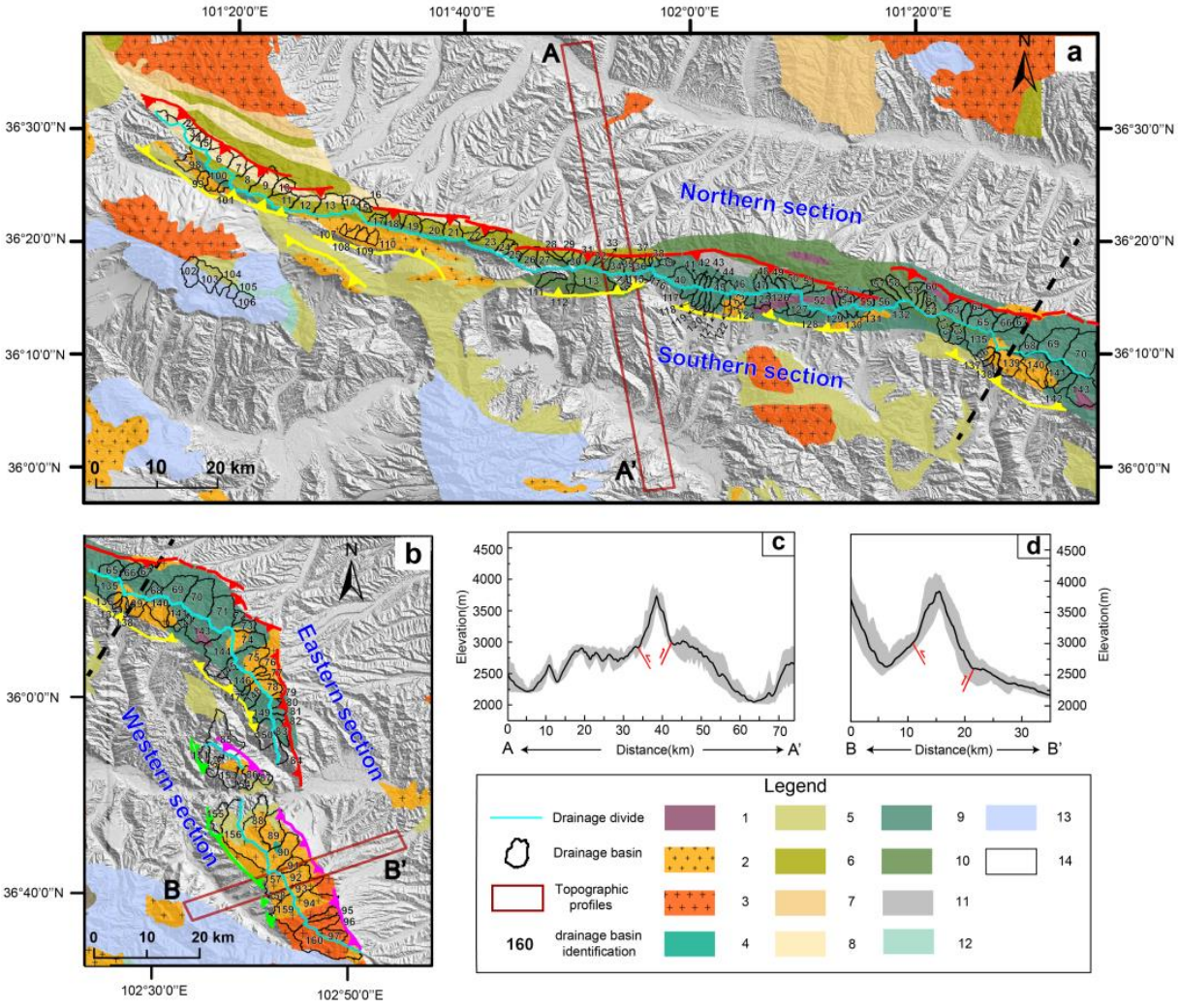

Figure 2. (**a**,**b**) The lithologic and drainage basin distribution map of the LJSFZ region (lithological information modified after Fu et al., 2018 [46]; the fault information is consistent with the legend in Figure 1b). (1. Mafic-ultramafic rock; 2. diorite; 3. granite; 4. peridotite; 5. Hualong Complex: gneiss, schist, and amphibolite; 6. Qingshipo Formation: phyllite and limestone; 7. Dongchagou Formation: schist, phyllite, and quartzite; 8. Huashishan Group: dolomite and limestone; 9. Cambrian volcano-sedimentary series; 10. Ordovician volcanic and sedimentary rocks; 11. Silurian sandstone and conglomerate; 12. Permian sedimentary rock; 13. Triassic sedimentary rock; 14. Jurassic–Quaternary sedimentary rock). The black dashed line represents the boundary between the northern-southern and eastern-western divisions. (**c**,**d**) The 4 km wide swath profiles of A-A′ and B-B′. The shaded area represents the range between the maximum and minimum elevation of the topographic profile, while the red line indicates the fault location.

3.1. Hypsometric Integral (HI)

The hypsometric integral (*HI*) reflects the distribution of area and elevation within a drainage basin, indicating the balance between tectonic uplift and erosion [47]. High *HI* values suggest dominant tectonic uplift, while low values indicate tectonic stability [48]. According to El Hamdouni et al. [49], *HI* values categorize tectonic activity as follows: $HI < 0.4$ signifies weak activity (old topography), $HI > 0.6$ indicates strong activity (young topography), and $0.4 \leq HI \leq 0.6$ represents moderate activity (mature topography) [50,51]. The *HI* is calculated as:

$$HI = (h_{mean} - h_{min})/(h_{max} - h_{min}), \quad (1)$$

In Equation (1), the h_{mean}, h_{max}, and h_{min} are the mean, maximum, and minimum elevations.

3.2. Stream Length Gradient (SL)

The stream length-gradient (*SL*) index measures variations in stream profiles, primarily influenced by tectonic activity, rock resistance, and topographic characteristics [52]. Higher *SL* values often correspond to areas of active tectonics or resistant rock, while lower values suggest weaker tectonic influence. Typically, $SL > 500$ indicates strong tectonic uplift, $SL < 300$ reflects weak uplift, and intermediate values indicate moderate activity [49,53,54].

In a drainage basin, the slope of a stream is steeper in the upper reaches and slower near the estuary. Therefore, the *SL* is calculated by multiplying the slope of each stream segment by the distance from the middle point of the stream segment to the source of the stream to amplify the *SL* of the downstream stream segment [22]. *SL* is calculated using the follow equation:

$$SL = (\Delta H/\Delta L) * L, \quad (2)$$

In Equation (2), ΔH is the elevation difference, ΔL is the length of the stream segment, and L is the horizontal distance from the drainage divide to the midpoint of the segment.

3.3. Channel Steepness Index (k_{sn})

The channel steepness index (k_{sn}) is a critical tool for assessing river incision in response to tectonic uplift, climate, and rock properties [55–57]. High k_{sn} values typically indicate regions strongly influenced by tectonic uplift, as streams in these areas exhibit steep gradients. Conversely, low k_{sn} values are associated with regions of low tectonic uplift [16,58–60]. For instance, regions with active thrust faults, like the northern Qilian Shan, show high k_{sn} values (>100), indicating significant uplift [61]. The k_{sn} is derived from the relationship:

$$S = k_{sn} A^{-\theta} \quad (3)$$

In Equation (3), S is the channel slope, A is the drainage area, k_{sn} is the channel steepness index, and θ is the concavity index. The index k_{sn} reflects the balance between uplift (U) and erosion (K), with θ = m/n representing the convexity of the channel profile.

4. Results

4.1. Geomorphic Analysis of Drainage Basins by Flow Direction

Based on the division of the 160 drainage basins into four directional categories—north (67), south (41), east (30), and west (22)—we conducted a comparative analysis of geomorphic indices across these regions using boxplots to visualize the variations (Figure 3). The hypsometric integral (*HI*) exhibited minimal variation across the four directions, with the boxplot widths being fairly consistent (ranging from 0.44 to 0.54) and the mean values showing negligible differences (between 0.49 and 0.51). This suggests that *HI* may not be a sensitive indicator of tectonic activity within this region (Figure 3a).

In contrast, the stream length-gradient index (*SL*) and channel steepness index (k_{sn}) demonstrated significant variability across the different directional basins (Figure 3b,c). The *SL* index was highest in the eastern basins (Table 2), with an average value of 589, nearly double that of the southern (314) (Table 3) and northern (319) basins (Table 1). The western basins also showed relatively high values (452) (Table 4). The boxplots for *SL* showed a clear pattern, with the eastern basins exhibiting the highest values, followed by the western basins, while the southern and northern basins showed the lowest values.

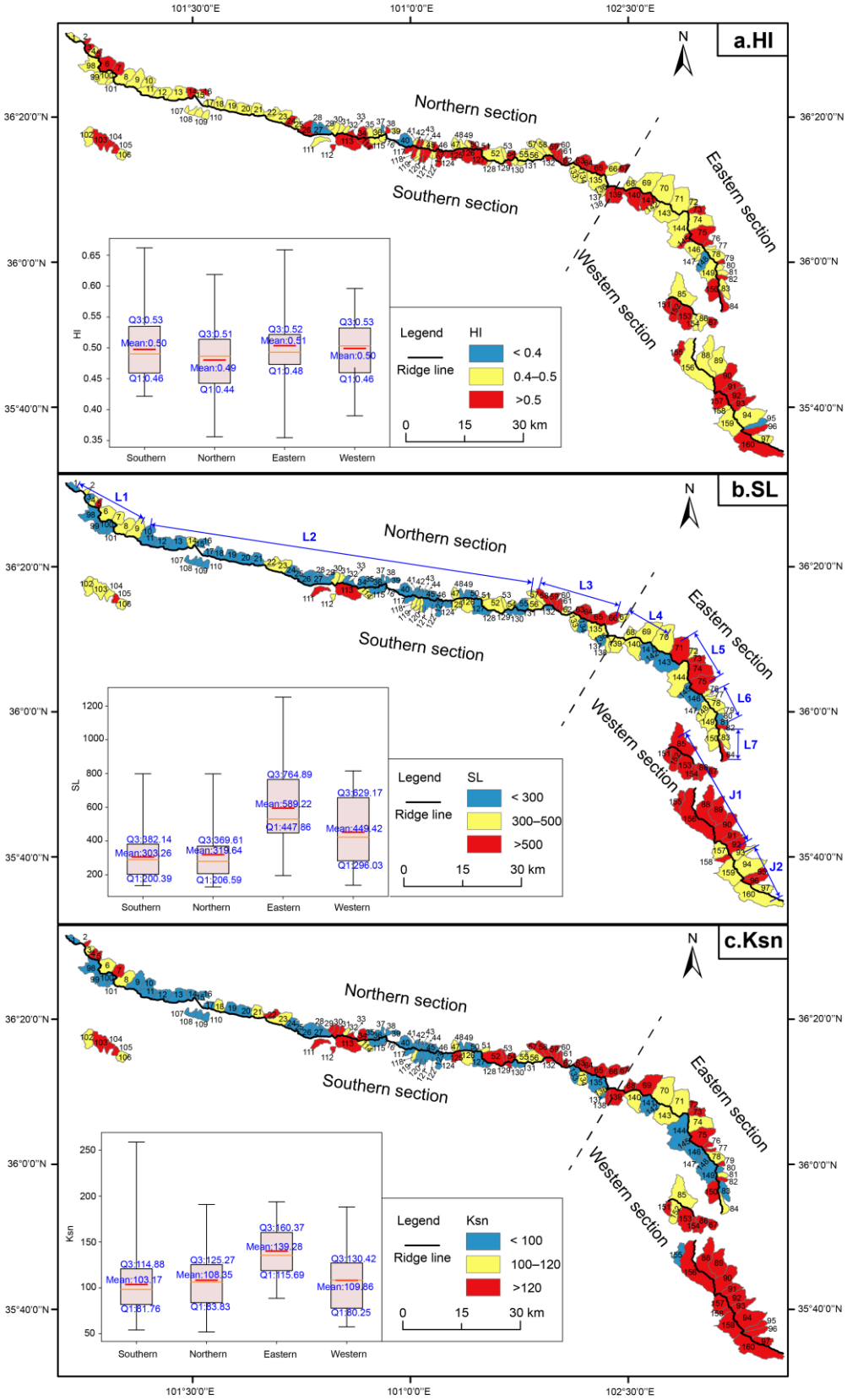

Figure 3. Geomorphic indices' distribution maps of the LJSFZ (with different colors representing varying levels of activity) and box-and-whisker diagrams (showing the means, medians, interquartile ranges, and data ranges). (**a**) *HI* distribution map, (**b**) *SL* distribution map and segmentation of fault activity along the northern and eastern sides of the LJFSZ, (**c**) k_{sn} distribution map.

The k_{sn} index displayed a similar distribution to *SL*, with the highest values observed in the eastern basins. However, unlike *SL*, k_{sn} did not show elevated values in the western basins; instead, the western basins' average k_{sn} was similar to those in the southern and northern basins, with the boxplots reflecting a comparable trend (Figure 3c).

In summary, the eastern basins of the LJSFZ exhibited the highest geomorphic index values, potentially indicating relatively higher uplift rates in this region. In contrast, the uplift rates in the other regions may be relatively lower.

To further distinguish the tectonic uplift differences across various segments of the LJSFZ, we conducted a more detailed segmentation analysis focusing on the northern Laji Shan faults and the eastern Jishi Shan faults, particularly in the northern and eastern basins. The decision to focus on these basins was based on two main reasons: firstly, the preliminary results indicate stronger tectonic activity in the eastern side; secondly, the northern and eastern basins together account for 97 of the 160 basins, forming the majority, and these basins are continuously distributed along the mountain range, providing a coherent and extensive area for detailed study.

4.2. Detailed Fault Segmentation in the Northern and Eastern LJSFZ

Building on our regional analysis of geomorphic indices, we conducted a detailed segmentation study focusing on the northern and eastern flanks of the LJSFZ. This analysis involved evaluating geomorphic indices from 84 drainage basins on the northern flanks of Laji Shan and 13 on the eastern flank of Jishi Shan. The stream length-gradient index (*SL*) and channel steepness index (k_{sn}) revealed significant trends across specific segments of these faults.

The analysis identified distinct segmentation characteristics, particularly through the variability in *SL* values. Using established classification criteria for tectonic activity intensity based on *SL*, we divided the northern Laji Shan faults into six segments (L1–L7) and the eastern Jishi Shan faults into two segments (J1 and J2). Among these, segments L3, L5, and L7 on Laji Shan exhibited the highest tectonic activity ($SL > 500$), while segments L4, L6, and L1 showed moderate activity ($300 < SL < 500$) and segment L2 demonstrated the weakest activity ($SL < 300$). The eastern Jishi Shan faults generally displayed higher *SL* values (>500), with segment J1 emerging as the most active across the entire LJSFZ (Figure 4b).

The spatial distribution of k_{sn} values on the northern Laji Shan faults largely mirrored the trends observed in *SL*. Segment L3 showed the highest k_{sn} values, indicating the strongest tectonic activity, while segment L2 had the lowest values, reflecting weaker tectonic activity. Similarly, the Jishi Shan segments, J1 and J2, exhibited notably high k_{sn} values, suggesting intense and relatively uniform tectonic activity across these segments (Figure 4c).

However, a detailed examination revealed that segments L4, L5, L6, and L7 had relatively consistent k_{sn} values, which contrasted with the significant variations in *SL* values across these segments. Upon comparing these segmentation results with changes in the fault strike, we observed that the boundaries between these segments corresponded with strike orientation shifts exceeding 20°, indicating clear tectonic segmentation. Based on this correlation, we chose to adopt the segmentation delineated by *SL* values, treating L4, L5, L6, and L7 as distinct segments (Figure 4d).

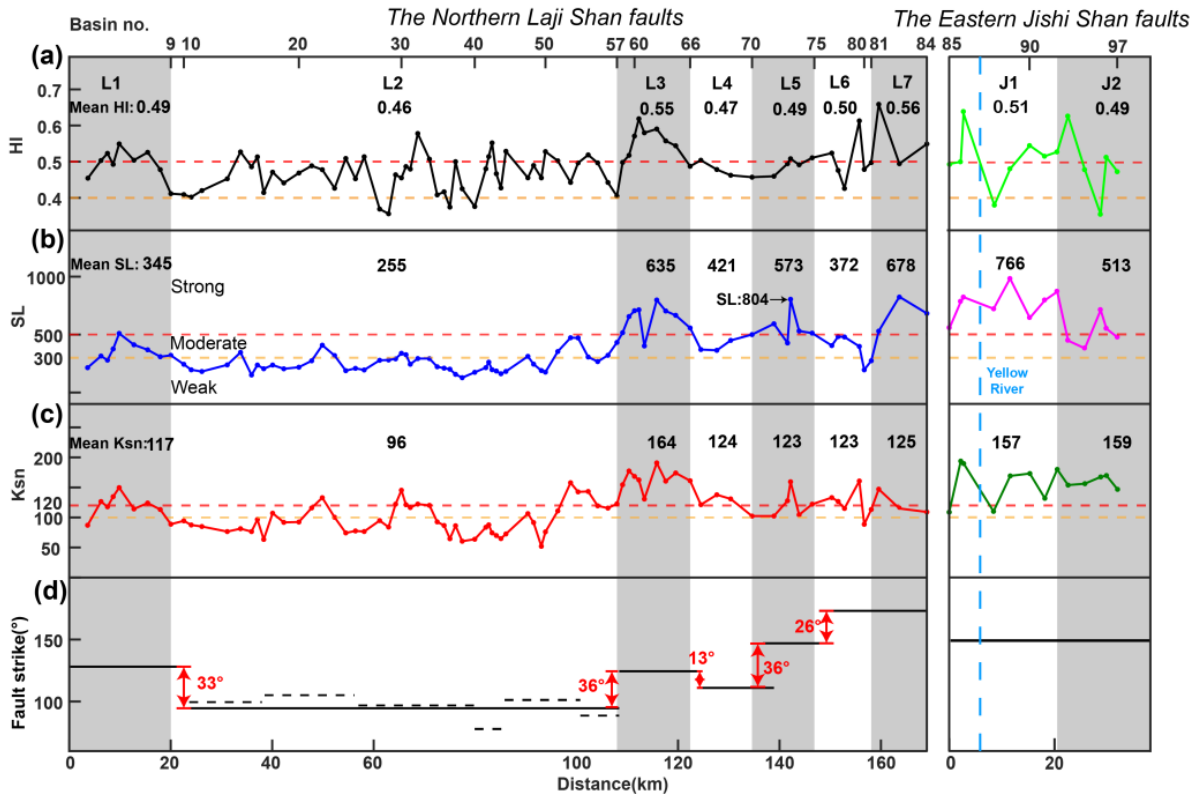

Figure 4. Comparison of geomorphic indices *HI*, *SL*, and k_{sn} on the northern Laji Shan and the eastern Jishi Shan faults; the red and yellow horizontal, dashed lines in panels. (**a**–**c**) represent the boundaries between strong, moderate, and weak tectonic activity based on El Hamdouni et al. [49]; the blue dashed line represents the location of the Yellow River; (**a**) variation of *HI* values along the mountain strike; (**b**) variation of *SL* values along the mountain strike; (**c**) variation of k_{sn} values along the mountain strike; (**d**) variations in the strike of the northern Laji Shan and eastern Jishi Shan faults.

4.3. Correlation between Uplift Rates and Geomorphic Indices in the LJSFZ

Using the highest-resolution, three-dimensional crustal velocity field data for the northeastern Tibetan Plateau, obtained through GNSS and InSAR joint inversion [43], we extracted seven vertical crustal deformation rate profiles across the Laji-Jishi Shan belt, targeting segments with varying tectonic activity. Each profile spanned 10 km, covering the Laji and Jishi Shan ranges and adjacent Cenozoic basins. We calculated the *SL* index for drainage basins within these profiles to explore the correlation between uplift rates and *SL* values, particularly in the basins north and east of the Laji and Jishi Shans (Figure 5a).

For high *SL* value segments, L3, L5, and J1 correspond to profiles 5-5′, 6-6′, and 7-7′, respectively (Figure 5b). In profile 5-5′, the uplift rate from the northern flank of Laji Shan to the center of Xining Basin is 3.14 ± 1.25 mm/yr, with an average *SL* value of 677. In profile 6-6′, the uplift rate is 3.04 ± 1.13 mm/yr, with an average *SL* value of 546. In profile 7-7′, the uplift rate from the eastern edge of Jishi Shan to the Linxia Basin center is 2.82 ± 1.18 mm/yr, with an average *SL* value of 811.

For moderate *SL* value segments, L1 corresponds to profile 1-1′, with an uplift rate of 2.64 ± 0.80 mm/yr and an average *SL* value of 352 (Figure 5b).

For low *SL* value segments, L2 corresponds to profiles 2-2′, 3-3′, and 4-4′. In profile 2-2′, the uplift rate is 2.15 ± 0.74 mm/yr, with an average *SL* value of 241. In profile 3-3′, the uplift rate is 1.97 ± 0.87 mm/yr, with an average *SL* value of 293. In profile 4-4′, the uplift rate is 1.97 ± 0.68 mm/yr, with an average *SL* value of 255 (Figure 5b).

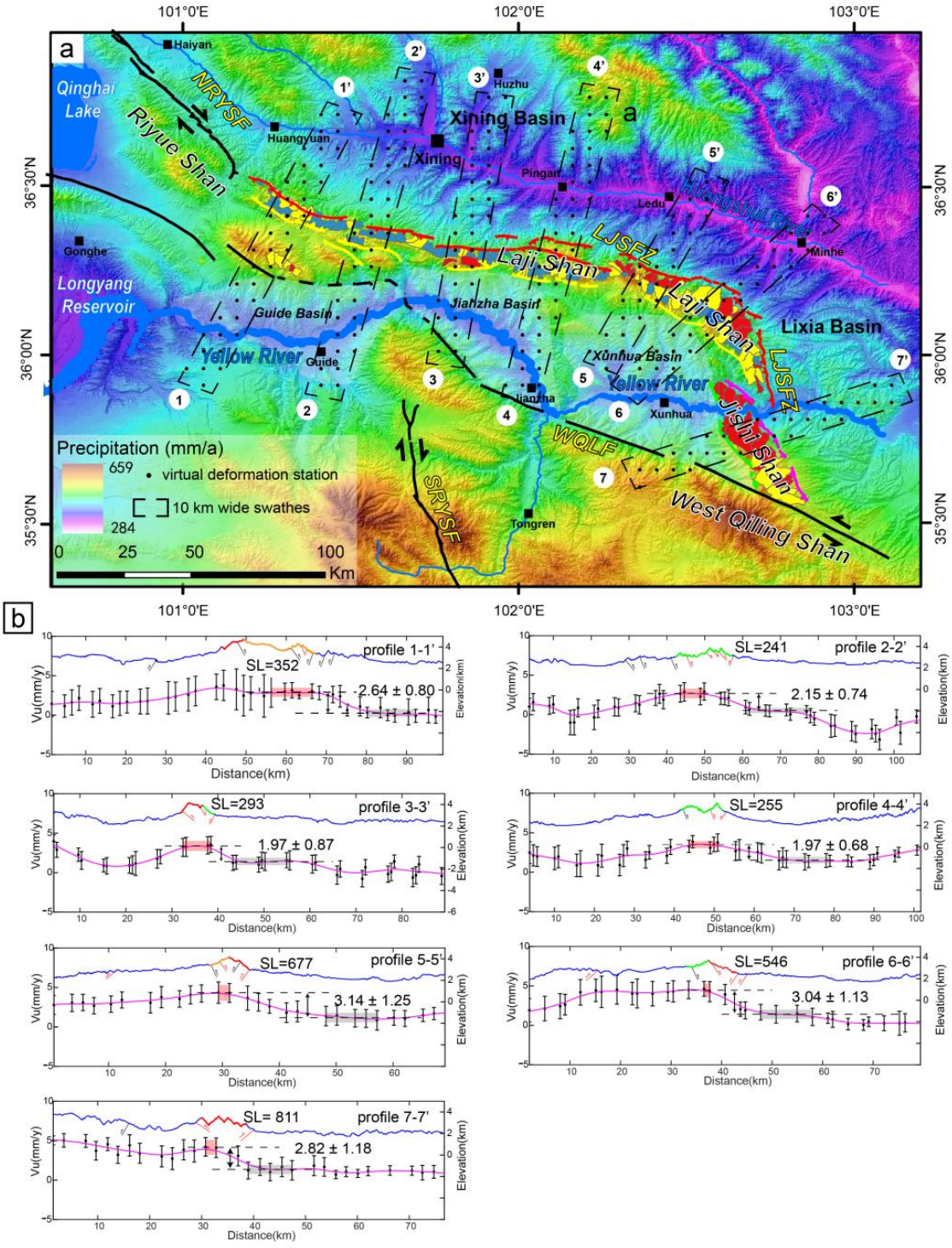

Figure 5. Vertical crustal deformation profiles across different segments of the LJSFZ; vertical velocity data from Wu et al., 2024 [43] and precipitation data: (**a**) location of the profiles and the average annual precipitation (mm/year) in the study area from 1970 to 2000 (obtained from: https://www.worldclim.org, accessed on 26 September 2024); (**b**) seven vertical crustal deformation profiles. In the topographic profiles, red, orange, and green represent high, medium, and low *SL* values for the drainage basins the profiles' cross, respectively. Red and black fault lines indicate Holocene active faults and Cenozoic faults. The black dots in the deformation profiles represent vertical uplift rates, with the purple line showing the fitted result of these points. The black dashed line indicates the average uplift rate for the maximum and minimum portions of the profile, while the red and gray squares represent the error ranges.

These profiles reveal a clear correlation between uplift rates and *SL* values. Segments with strong tectonic activity, such as L3, L5, and J1, exhibit higher uplift rates (~3 mm/yr), while segments with weaker activity, like L2, show lower rates (~2 mm/yr). Segments with moderate activity, like L1, have intermediate uplift rates (2–3 mm/yr). Correlation analysis shows a significant positive relationship between uplift rates and *SL* values (correlation coefficient of 0.84), indicating that geomorphic indices effectively reflect fault activity intensity. The relationship suggests that when *SL* > 500, the uplift rate typically exceeds 2.60 mm/yr, indicating strong tectonic activity (Figure 6).

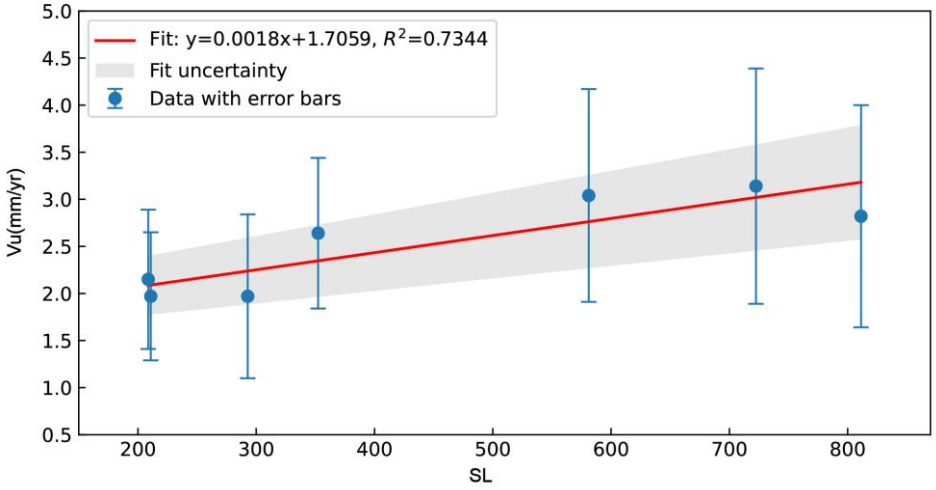

Figure 6. *SL* Values and Vu (uplift rates) linear fit.

However, the current dataset is limited, and further verification is needed to ensure the accuracy and applicability of this quantitative relationship. Additionally, the uplift rates derived from the deformation profiles may reflect the combined effects of the piedmont fault and basin sedimentation zones. Erosion of the mountain range and sedimentation in the basin may introduce uncertainty into the vertical crustal deformation rate data.

5. Discussion

5.1. Segmented Results and Uncertainty

Rainfall and lithological variations significantly influence geomorphic indices [62], introducing uncertainties that need to be addressed. *HI* values, in particular, exhibit notable spatial and area dependency [63]. In small drainage basins, lithology predominantly influences *HI* values, while in larger basins, tectonic factors have a more pronounced effect. Although threshold values may vary among different basins, it is widely accepted that basin area influences *HI* values. Our results showed that in some small basins (e.g., basins 125, 126, 127, etc., <3 km^2), *HI* values diverged significantly from *SL* and k_{sn} values, suggesting that *HI* in these cases may reflect lithological differences rather than tectonic activity. This likely contributes to the lower correlation between *HI* and the other geomorphic indices.

Erosional resistance of bedrock varies with rock type, theoretically affecting *SL* as rivers traverse different units [52]. However, Figure 2 shows that high *SL* values do not consistently align with lithologies of high erosional resistance. Unexpectedly, high *SL* values are observed not only in resistant rock units such as granite, diorite, and gneiss (e.g., basins 63–66 and 88–92) but also in moderately resistant units like dolomite (e.g., basin 5) and even in low-resistance lithologies such as sandstone and conglomerate (e.g., basins 151–154). Furthermore, some rock units with very high erosional resistance do not display higher *SL* values compared to those with lower resistance. Thus, lithology's impact on *SL* values in the study area appears limited, with a similarly weak correlation between k_{sn} and lithological variations. Consequently, no clear pattern or correlation exists among *SL*, k_{sn} values, and lithology in the study area.

We collected rainfall data for the period 1970–2000 from WorldClim (https://www.worldclim.org, accessed on 26 September 2024) (Figure 7a). Overall, the study area experiences a plateau continental climate dominated by westerly winds, resulting in cold and dry conditions, with an average annual rainfall between 420 and 620 mm in LJSFZ [64]. Given this, climate is unlikely to be a primary factor influencing geomorphic indices. Instead, variations in these indices are primarily driven by the intensity of mountain uplift, with lithology and climate playing only a minor role.

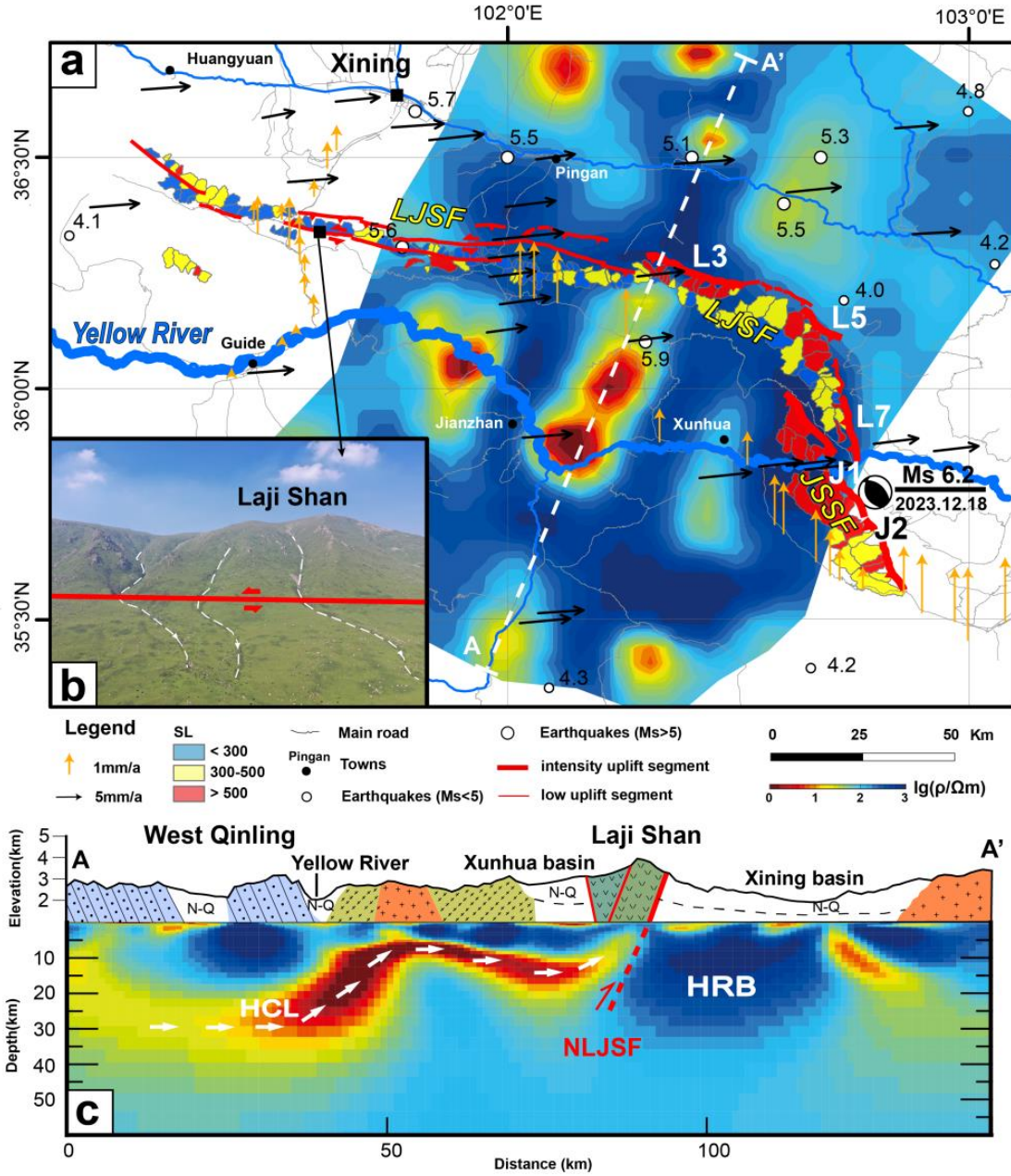

Figure 7. Crustal deformation field and electrical structure: (**a**) GNSS velocity field (horizontal black arrows) and leveling data (vertical yellow arrow) from Zhuang et al., 2023 [65], along with subsurface electrical structure at 10 km depth from Zhao et al., 2022 [38], The white dashed line is the profile line; (**b**) left-lateral strike-slip movement along the Laji Shan fault; (**c**) cross-section A-A′ topographic profile, adapted from [46], the lithology fill is consistent with Figure 2. HCL refers to the high-conductivity layer, HRB refers to the high-resistivity body, and NLJSF refers to the North Laji Shan fault.

5.2. Segmentation and the Role of the Yellow River Valley in the Eastern Jishi Shan Faults

The 2023 Ms 6.2 Jishi Shan earthquake, a thrust fault event, occurred in the J1 segment of the LJSFZ, where the most pronounced geomorphic uplift is observed along the fault zone. This correlation indicates that the segmentation of geomorphic indices aligns with current seismic activity patterns. Notably, no significant surface ruptures were observed during the earthquake, and both the mainshock and aftershocks were primarily located in the Jishi Shan piedmont, south of the Yellow River [43]. Some researchers have suggested a fault structure along the Yellow River valley may delineate distinct seismic units between the northern and southern sides [66,67].

However, our analysis of geomorphic indices shows that the entire eastern flank of Jishi Shan, particularly in the eight drainage basins (85–92) within the J1 segment, exhibits high *SL* values ranging from 643 to 979 (Table 2 and Figure 4b). There is no significant difference in *SL* values between the northern and southern sides of the Yellow River. Therefore, we propose that the Yellow River valley does not serve as an active segmentation boundary within the eastern Jishi Shan faults.

5.3. The Dynamic Mechanism of LJSFZ Segmentation

The uplift intensity of the Laji-Jishi Shan belt varies, with weaker uplift in the northern and southern basins and stronger uplift in the southward-curving eastern and western basins. This pattern is likely influenced by the regional principal stress direction. Recent data inversion indicates a NEE-oriented principal stress in the LJSFZ area, aligning with the current GNSS deformation field (Figure 7a) [43,65]. This stress orientation is nearly perpendicular to the NNW-trending Jishi Shan and the eastern segment of Laji Shan, contributing to the pronounced uplift observed there. In contrast, the western segment of the Laji Shan intersects the principal stress at a more oblique angle, favoring strike-slip motion over significant uplift. High-precision leveling data show that the uplift rate in the Jishi Shan segment was 3–4 times greater than in the western end of Laji Shan from 1970 to 2012 (Figure 7a). Geological and geomorphological surveys, supported by remote sensing, confirm significant left-lateral strike-slip motion in the western segment of Laji Shan, with rivers, ridges, and terraces exhibiting varying degrees of horizontal displacement (Figure 7b) [15].

Despite its near-parallel alignment with the regional GNSS deformation field, the L3 segment of western Laji Shan exhibits the most intense uplift across the entire range, as indicated by geomorphological indices (Figure 7a). This uplift is likely influenced by deep crustal processes, particularly the migration of crustal material. A 3D deep electrical structure survey revealed a significant, continuous zone of high conductivity (low resistivity) in the middle to lower crust, located 25 km south of Laji Shan (Figure 7c). This feature, similar to those found in the Tibetan Plateau interior, is typically interpreted as "lower crustal flow", which drives deformation and outward expansion of the Plateau [68–70].

While the resistivity maps at different depths (Figure 7a) may suggest these zones as separate high-conductivity bodies, our interpretation, based on the A-A′ cross-section, suggests that they form a locally continuous low-resistivity structure. Zhao et al. (2022) [38] describe this low-resistivity body as migrating from south to north, ascending from deeper to shallower levels, and being obstructed by a high-resistivity body beneath the Xining Basin (Figure 7c). This obstruction likely causes the concentrated uplift observed at the L3 segment.

This interpretation is further supported by seismic and heat flow data, which suggest partial crustal melting consistent with the observed low-resistivity zone. Specifically, studies in the Gonghe Basin (Figure 1b), approximately 90 km southwest of Laji Shan, report exceptionally high heat flow values of up to 119.3 mW/m^2—about 1.6 times the background level of the Tibetan Plateau [71]. These values suggest temperatures at the Moho that could reach 2690 °C, implying partial melting at depths of 12–13 km, which aligns with the depth of the low-resistivity body observed in the A-A′ profile (Figure 7c).

Although the direction of this localized crustal flow (NNE) differs from the broader regional GNSS deformation field (NEE), such deviations are plausible, particularly at the margins of the Tibetan Plateau where local geodynamic conditions may dominate. In the interior regions of the plateau, the movement of low-resistivity bodies generally aligns with the surface velocity field [72,73]. However, at the plateau's margins, where low-resistivity bodies encounter high-resistivity barriers like the Xining Basin, the flow becomes more localized and directed toward the plateau margins. This localized, small-scale crustal flow, while not perfectly aligned with the broader surface velocity field, could still drive significant localized uplift and enhance fault activity.

The current crustal deformation characteristics align with the activity segmentation identified in this study, indicating consistent stress–strain patterns over both long-term (Ma) and short-term (10 a) timescales. Additionally, deep crustal electrical structures suggest that the LJSFZ acts as a physical boundary impeding the outward expansion of the highly conductive middle to lower crust of the Tibetan Plateau [38]. This supports the conclusion that the Laji-Jishi Shan tectonic belt, as a primary structure accommodating regional stress and strain, has historically been—and is likely to continue being—a significant seismogenic zone for strong earthquakes.

6. Conclusions

This study analyzes tectonic activity of different segments within the LJSFZ by integrating geomorphic indices, cross-fault deformation rate profiles, and 3D crustal electrical structure data. The results indicate that the eastern basins of the LJSFZ exhibit the strongest tectonic activity, with significant variations in SL and k_{sn} indices along the fault strike, highlighting clear fault segmentation characteristics. Segment J1 emerges as the most active within the entire LJSFZ, consistent with recent significant earthquakes in the region. These segmentation features are further validated by comparisons with cross-fault deformation data, demonstrating that geomorphic indices effectively reflect fault activity intensity. Additionally, 3D electrical structure data reveal that the high-conductivity middle- to lower-crustal material from the interior of the Tibetan Plateau is obstructed at segment L3 of the LJSFZ, leading to localized intense uplift and increased fault activity. The stress–strain pattern in the northeastern Tibetan Plateau is the primary driver of segmented activity in the Laji-Jishi Shan belt, with the localized crustal flow playing a critical role in influencing fault segmentation.

Author Contributions: Conceptualization, methodology, software, writing—original draft preparation, Y.M. and W.H.; supervision, validation, resources, B.P.; visualization, data curation, J.Z., Y.W. and D.Y. All authors have read and agreed to the published version of the manuscript.

Funding: This study was supported by the National Natural Science Foundation of China (Grant No. 42041006, 42277152), the Fundamental Research Funds for the Central Universities, Chang'an University (300102264908), and was partly supported by the Shaanxi Province Science and Technology Innovation Team (Ref. 2021TD-51) and the innovation team of ShaanXi Provincial Tri-Qin Scholars with Geoscience Big Data and Geohazard Prevention (2022); and the Observation and Research Station of Ground Fissure and Land Subsidence, Ministry of Natural Resources (GKF2024-04).

Data Availability Statement: For relevant data, please contact the corresponding author.

Acknowledgments: We thank the reviewers and editors for their assistance in improving our manuscript.

Conflicts of Interest: The authors declare no conflicts of interest.

References

1. Zhang, P.; Slemmons, D.B.; Mao, F. Geometric pattern, rupture termination and fault segmentation of the Dixie Valley—Pleasant Valley active normal fault system, Nevada, USA. *J. Struct. Geol.* **1991**, *13*, 165–176. [CrossRef]
2. Zhang, P.; Mao, F.; Slemmons, D.B. Rupture terminations and size of segment boundaries from historical earthquake ruptures in the Basin and Range Province. *Tectonophysics* **1999**, *308*, 37–52. [CrossRef]
3. Milliner, C.W.; Dolan, J.F.; Hollingsworth, J.; Leprince, S.; Ayoub, F.; Sammis, C.G. Quantifying near-field and off-fault deformation patterns of the 1992 Mw 7.3 L anders earthquake. *Geochem. Geophys. Geosyst.* **2015**, *16*, 1577–1598. [CrossRef]

4. Klinger, Y.; Michel, R.; King, G.C. Evidence for an earthquake barrier model from Mw~ 7.8 Kokoxili (Tibet) earthquake slip-distribution. *Earth Planet. Sci. Lett.* **2006**, *242*, 354–364. [CrossRef]
5. Wesnousky, S.G. Predicting the endpoints of earthquake ruptures. *Nature* **2006**, *444*, 358–360. [CrossRef]
6. Scholz, C.H. *The Mechanics of Earthquakes and Faulting*; Cambridge University Press: Cambridge, UK, 2019.
7. Manighetti, I.; Zigone, D.; Campillo, M.; Cotton, F. Self-similarity of the largest-scale segmentation of the faults: Implications for earthquake behavior. *Earth Planet. Sci. Lett.* **2009**, *288*, 370–381. [CrossRef]
8. Wesnousky, S.G. Seismological and structural evolution of strike-slip faults. *Nature* **1988**, *335*, 340–343. [CrossRef]
9. Craddock, W.H.; Kirby, E.; Harkins, N.W.; Zhang, H.; Shi, X.; Liu, J. Rapid fluvial incision along the Yellow River during headward basin integration. *Nat. Geosci.* **2010**, *3*, 209–213. [CrossRef]
10. Wang, E.; Shi, X.; Wang, G.; Fan, C. Structural control on the topography of the Laji-Jishi and Riyue Shan belts in the NE margin of the Tibetan plateau: Facilitation of the headward propagation of the Yellow River system. *J. Asian Earth Sci.* **2011**, *40*, 1002–1014. [CrossRef]
11. Lease, R.O.; Burbank, D.W.; Zhang, H.; Liu, J.; Yuan, D. Cenozoic shortening budget for the northeastern edge of the Tibetan Plateau: Is lower crustal flow necessary? *Tectonics* **2012**, *31*, TC3011. [CrossRef]
12. Yuan, D.-Y.; Ge, W.-P.; Chen, Z.-W.; Li, C.-Y.; Wang, Z.-C.; Zhang, H.-P.; Zhang, P.-Z.; Zheng, D.-W.; Zheng, W.-J.; Craddock, W.H.; et al. The growth of northeastern Tibet and its relevance to large-scale continental geodynamics: A review of recent studies. *Tectonics* **2013**, *32*, 1358–1370. [CrossRef]
13. Huang, X.; Li, Y.; Shan, X.; Zhong, M.; Wang, X.; Gao, Z. Fault Kinematics of the 2023 Mw 6.0 Jishishan Earthquake, China, Characterized by Interferometric Synthetic Aperture Radar Observations. *Remote Sens.* **2024**, *16*, 1746. [CrossRef]
14. Yuan, D.Y.; Zhang, P.Z.; Lei, Z.S.; Liu, B.C.; Liu, X.L. A Preliminary Study on the New Activity Features of the Lajishan Mountain Fault Zone in Qinghai Province. *Earthq. Res. China* **2005**, *21*, 93–102.
15. Zhimin, L.; Qinjian, T.; Hongwei, T. Remote Sensing Characteristics of Laji Shan Fault. *Plateau Earthq. Res.* **2009**, *21*, 26–31.
16. Kirby, E.; Whipple, K. Quantifying differential rock-uplift rates via stream profile analysis. *Geology* **2001**, *29*, 415–418. [CrossRef]
17. Cheng, Y.; He, C.; Rao, G.; Yan, B.; Lin, A.; Hu, J.; Yu, Y.; Yao, Q. Geomorphological and structural characterization of the southern Weihe Graben, central China: Implications for fault segmentation. *Tectonophysics* **2018**, *722*, 11–24. [CrossRef]
18. Huang, W.; Lv, Y.; Pierce, I.K.D.; Su, S.; Peng, J. Cosmogenic age constraints on rock avalanches in the Qinling Range associated with paleoearthquake activity, central China. *Geomorphology* **2022**, *413*, 108347. [CrossRef]
19. Gao, M.; Hao, M.; Zeilinger, G.; Xu, X. Recent Uplift Characteristics of the Southeast Tibetan Plateau, an Analysis Based on Fluvial Indices. *Remote Sens.* **2023**, *15*, 433. [CrossRef]
20. Guo, L.; He, Z.; Li, L. Responses of Stream Geomorphic Indices to Piedmont Fault Activity in the Northern Segment of the Red River Fault Zone. *Remote Sens.* **2023**, *15*, 988. [CrossRef]
21. Shen, K.; Dong, S.; Wang, Y. Active Tectonics Assessment Using Geomorphic and Drainage Indices in the Sertengshan, Hetao Basin, China. *Remote Sens.* **2023**, *15*, 3230. [CrossRef]
22. Xu, D.; He, Z.; Guo, L.; Wu, L.; Li, L. Response of the Stream Geomorphic Index to Fault Activity in the Lianfeng–Ningnan Segment (LNS) of the Lianfeng Fault on the Eastern Margin of the Tibetan Plateau. *Remote Sens.* **2023**, *15*, 2309. [CrossRef]
23. Qureshi, K.A.; Khan, S.D. Active Tectonics of the Frontal Himalayas: An Example from the Manzai Ranges in the Recess Setting, Western Pakistan. *Remote Sens.* **2020**, *12*, 3362. [CrossRef]
24. Giona Bucci, M.; Schoenbohm, L.M. Tectono-Geomorphic Analysis in Low Relief, Low Tectonic Activity Areas: Case Study of the Temiskaming Region in the Western Quebec Seismic Zone (WQSZ), Eastern Canada. *Remote Sens.* **2022**, *14*, 3587. [CrossRef]
25. Ji, T.; Zheng, W.; Yang, J.; Zhang, D.; Liang, S.; Li, Y.; Liu, T.; Zhou, H.; Feng, C. Tectonic Significances of the Geomorphic Evolution in the Southern Alashan Block to the Outward Expansion of the Northeastern Tibetan Plateau. *Remote Sens.* **2022**, *14*, 6269. [CrossRef]
26. Zhang, P.-Z. A review on active tectonics and deep crustal processes of the Western Sichuan region, eastern margin of the Tibetan Plateau. *Tectonophysics* **2013**, *584*, 7–22. [CrossRef]
27. Fang, P.; Hou, G. Channel flow and fault segmentation with implications for the generation of earthquakes in the Longmenshan fault zone, eastern Tibetan Plateau. *J. Asian Earth Sci.* **2019**, *177*, 107–116. [CrossRef]
28. Cao, S.; Neubauer, F. Deep crustal expressions of exhumed strike-slip fault systems: Shear zone initiation on rheological boundaries. *Earth-Sci. Rev.* **2016**, *162*, 155–176. [CrossRef]
29. Huang, W.; Yang, X.; Thompson Jobe, J.A.; Li, S.; Yang, H.; Zhang, L. Alluvial plains formation in response to 100-ka glacial–interglacial cycles since the Middle Pleistocene in the southern Tian Shan, NW China. *Geomorphology* **2019**, *341*, 86–101. [CrossRef]
30. *GB18306-2015*; Seismic Ground Motion Parameters Zonation Map of China. National Seismic Standardization Technical Committee: Beijing, China, 2015.
31. Bo, Z. *The Study of New Activities on Western Segment of Northern Margin of Western Qinling Fault and Laji Shan Fault*; Lanzhou Institute of Seismology, CEA: Lanzhou, China, 2012; pp. 86–98.
32. Cheng, J.; Rong, Y.; Magistrale, H.; Chen, G.; Xu, X. An Mw-Based Historical Earthquake Catalog for Mainland China. *Bull. Seismol. Soc. Am.* **2017**, *107*, 2490–2500. [CrossRef]
33. Molnar, P.; Tapponnier, P. Cenozoic tectonics of Asia: Effects of a continental collision. *Science* **1975**, *189*, 419–426. [CrossRef]
34. Zhang, P.-Z.; Shen, Z.; Wang, M.; Gan, W.; Bürgmann, R.; Molnar, P.; Wang, Q.; Niu, Z.; Sun, J.; Wu, J.; et al. Continuous deformation of the Tibetan Plateau from global positioning system data. *Geology* **2004**, *32*, 809–812. [CrossRef]
35. Zuza, A.V. *Tectonic Evolution of the Northeastern Tibetan Plateau*; University of California: Los Angeles, CA, USA, 2016.

36. Cheng, F.; Zuza, A.V.; Haproff, P.J.; Wu, C.; Neudorf, C.; Chang, H.; Li, X.; Li, B. Accommodation of India–Asia convergence via strike-slip faulting and block rotation in the Qilian Shan fold–thrust belt, northern margin of the Tibetan Plateau. *J. Geol. Soc.* **2021**, *178*, jgs2020-207. [CrossRef]
37. Zheng, W.; Liu, X.; Yu, J.; Yuan, D.; Zhang, P.; Ge, W.; Pang, J.; Liu, B. Geometry and late Pleistocene slip rates of the Liangdang-Jiangluo fault in the western Qinling mountains, NW China. *Tectonophysics* **2016**, *687*, 1–13. [CrossRef]
38. Zhao, L.; Zhan, Y.; Wang, Q.; Sun, X.; Hao, M.; Zhu, Y.; Han, J. 3D electrical structure and crustal deformation of the Lajishan Tectonic Belt, Northeastern margin of the Tibetan Plateau. *J. Asian Earth Sci.* **2022**, *224*, 104953. [CrossRef]
39. Lease, R.O.; Burbank, D.W.; Clark, M.K.; Farley, K.A.; Zheng, D.; Zhang, H. Middle Miocene reorganization of deformation along the northeastern Tibetan Plateau. *Geology* **2011**, *39*, 359–362. [CrossRef]
40. Lease, R.O.; Burbank, D.W.; Hough, B.; Wang, Z.; Yuan, D. Pulsed Miocene range growth in northeastern Tibet: Insights from Xunhua Basin magnetostratigraphy and provenance. *Bulletin* **2012**, *124*, 657–677. [CrossRef]
41. Hough, B.G.; Garzione, C.N.; Wang, Z.; Lease, R.O.; Burbank, D.W.; Yuan, D. Stable isotope evidence for topographic growth and basin segmentation: Implications for the evolution of the NE Tibetan Plateau. *Bulletin* **2011**, *123*, 168–185. [CrossRef]
42. Perrineau, A.; Woerd, J.V.D.; Gaudemer, Y.; Liu-Zeng, J.; Pik, R.; Tapponnier, P.; Thuizat, R.; Rongzhang, Z. Incision rate of the Yellow River in Northeastern Tibet constrained by 10Be and 26Al cosmogenic isotope dating of fluvial terraces: Implications for catchment evolution and plateau building. *Geol. Soc. Lond. Spec. Publ.* **2011**, *353*, 189–219. [CrossRef]
43. Wu, D.-L.; Ge, W.-P.; Liu, S.-Z.; Yuan, D.-Y.; Zhang, B.; Wei, C.-M. Present-Day 3D Crustal Deformation of the Northeastern Tibetan Plateau From Space Geodesy. *Geophys. Res. Lett.* **2024**, *51*, e2023GL106143. [CrossRef]
44. Wang, J.; He, Z. Responses of Stream Geomorphic Indices to Piedmont Fault Activity in the Daqingshan Area of China. *J. Earth Sci.* **2020**, *31*, 978–987. [CrossRef]
45. Shi, X.; Yang, Z.; Dong, Y.; Qu, H.; Zhou, B.; Cheng, B. Geomorphic indices and longitudinal profile of the Daba Shan, northeastern Sichuan Basin: Evidence for the late Cenozoic eastward growth of the Tibetan Plateau. *Geomorphology* **2020**, *353*, 107031. [CrossRef]
46. Fu, C.; Yan, Z.; Wang, Z.; Buckman, S.; Aitchison, J.C.; Niu, M.; Cao, B.; Guo, X.; Li, X.; Li, Y.; et al. Lajishankou Ophiolite Complex: Implications for Paleozoic Multiple Accretionary and Collisional Events in the South Qilian Belt. *Tectonics* **2018**, *37*, 1321–1346. [CrossRef]
47. Strahler, A.N. Hypsometric (Area-Altitude) Analysis of Erosional Topography. *GSA Bull.* **1952**, *63*, 1117–1142. [CrossRef]
48. Keller, E.A.; Pinter, N. *Active Tectonics Earthquakes, Uplift, and Landscape*, 2nd ed.; Prentice Hall: Upper Saddle River, NJ, USA, 2002.
49. El Hamdouni, R.; Irigaray, C.; Fernández, T.; Chacón, J.; Keller, E.A. Assessment of relative active tectonics, southwest border of the Sierra Nevada (southern Spain). *Geomorphology* **2008**, *96*, 150–173. [CrossRef]
50. Zhang, T.; Fan, S.; Chen, S.; Li, S.; Lu, Y. Geomorphic evolution and neotectonics of the Qianhe River Basin on the southwest margin of the Ordos Block, North China. *J. Asian Earth Sci.* **2019**, *176*, 184–195. [CrossRef]
51. Putra, A.F.; Chenrai, P. Relative tectonic activity assessment of the Northern Sumatran Fault using geomorphic indices. *Front. Southeast Asian Geosci.* **2022**, *10*, 969170. [CrossRef]
52. Hack, J.T. Stream-Profile analysis and stream-gradient index. *Bull. Am. Astron. Soc.* **1973**, *1*, 421–429.
53. Pourali, M.; Hoseynzadeh, R.; Akbari, M. Quantitative analysis of relative active tectonics using geomorphic indices in Band-Golestan basin, northeastern Iran. *Spat. Inf. Res.* **2020**, *28*, 419–429. [CrossRef]
54. Othman, A.T.; Omar, A.A. Evaluation of relative active tectonics by using geomorphic indices of the Bamo anticline, Zagros Fold-Thrust Belt, Kurdistan Region of Iraq. *Heliyon* **2023**, *9*, e17970. [CrossRef]
55. Kirby, E.; Whipple, K.X. Expression of active tectonics in erosional landscapes. *J. Struct. Geol.* **2012**, *44*, 54–75. [CrossRef]
56. Liu, F.; Yao, X.; Li, L. Applicability of Geomorphic Index for the Potential Slope Instability in the Three River Region, Eastern Tibetan Plateau. *Sensors* **2021**, *21*, 6505. [CrossRef] [PubMed]
57. Wang, J.; Hu, Z.; Pan, B.; Li, M.; Dong, Z.; Li, X.; Li, X.; Bridgland, D. Spatial distribution pattern of channel steepness index as evidence for differential rock uplift along the eastern Altun Shan on the northern Tibetan Plateau. *Glob. Planet. Chang.* **2019**, *181*, 102979. [CrossRef]
58. Whipple, K.X.; Tucker, G.E. Dynamics of the stream-power river incision model: Implications for height limits of mountain ranges, landscape response timescales, and research needs. *J. Geophys. Res. Solid Earth* **1999**, *104*, 17661–17674. [CrossRef]
59. Snyder, N.P.; Whipple, K.X.; Tucker, G.E.; Merritts, D.J. Landscape response to tectonic forcing: Digital elevation model analysis of stream profiles in the Mendocino triple junction region, northern California. *GSA Bull.* **2000**, *112*, 1250–1263. [CrossRef]
60. Wobus, C.; Whipple, K.X.; Kirby, E.; Snyder, N.; Johnson, J.; Spyropolou, K.; Crosby, B.; Sheehan, D. Tectonics from topography: Procedures, promise, and pitfalls. In *Tectonics, Climate, and Landscape Evolution*; Willett, S.D., Hovius, N., Brandon, M.T., Fisher, D.M., Eds.; Geological Society of America: Boulder, CO, USA, 2006; Volume 398, pp. 55–74.
61. Groves, K.; Saville, C.; Hurst, M.D.; Jones, S.J.; Song, S.G.; Allen, M.B. Geomorphic expressions of collisional tectonics in the Qilian Shan, north eastern Tibetan Plateau. *Tectonophysics* **2020**, *788*, 228503. [CrossRef]
62. Lifton, N.A.; Chase, C.G. Tectonic, climatic and lithologic influences on landscape fractal dimension and hypsometry: Implications for landscape evolution in the San Gabriel Mountains, California. *Geomorphology* **1992**, *5*, 77–114. [CrossRef]
63. Tarboton, D.G.; Bras, R.L.; Rodríguez-Iturbe, I. On the extraction of channel networks from digital elevation data. *Hydrol. Process.* **1991**, *5*, 81–100. [CrossRef]

64. Chen, F.; Zhang, J.; Liu, J.; Cao, X.; Hou, J.; Zhu, L.; Xu, X.; Liu, X.; Wang, M.; Wu, D. Climate change, vegetation history, and landscape responses on the Tibetan Plateau during the Holocene: A comprehensive review. *Quat. Sci. Rev.* **2020**, *243*, 106444. [CrossRef]
65. Zhuang, W.; Cui, D.; Hao, M.; Song, S.; Li, Z. Geodetic constraints on contemporary three-dimensional crustal deformation characteristics in the Laji Shan–Jishi Shan tectonic belt. *Geod. Geodyn.* **2023**, *14*, 589–596. [CrossRef]
66. Wang, S.; Xu, G.; Li, S.; Yang, T.; Shi, L.; Zhang, L.; Tang, F.; Fang, L. Analysis of earthquake sequence and seismogenic structure of the 2023 MS6.2 Jishishan earthquake, Gansu Province, China. *Acta Seismol. Sin.* **2024**, *46*, 1–16.
67. Yang, P.X.; Xiong, R.W.; Hu, Z.Z. Preliminary Analysis of the Seismogenic Tectonics for the 2023 Jishishan MS6.2 Earthquake in Gansu Province. *Earthquake* **2024**, *44*, 153–159.
68. Bai, D.; Unsworth, M.J.; Meju, M.A.; Ma, X.; Teng, J.; Kong, X.; Sun, Y.; Sun, J.; Wang, L.; Jiang, C.; et al. Crustal deformation of the eastern Tibetan plateau revealed by magnetotelluric imaging. *Nat. Geosci.* **2010**, *3*, 358–362. [CrossRef]
69. Zhao, G.; Unsworth, M.J.; Zhan, Y.; Wang, L.; Chen, X.; Jones, A.G.; Tang, J.; Xiao, Q.; Wang, J.; Cai, J.; et al. Crustal structure and rheology of the Longmenshan and Wenchuan Mw 7.9 earthquake epicentral area from magnetotelluric data. *Geology* **2012**, *40*, 1139–1142. [CrossRef]
70. Sun, X.; Zhan, Y.; Unsworth, M.; Egbert, G.; Zhang, H.; Chen, X.; Zhao, G.; Sun, J.; Zhao, L.; Cui, T. 3-D Magnetotelluric imaging of the easternmost Kunlun fault: Insights into strain partitioning and the seismotectonics of the Jiuzhaigou Ms7.0 earthquake. *J. Geophys. Res. Solid Earth* **2020**, *125*, e2020JB019731. [CrossRef]
71. Zhang, C.; Jiang, G.; Shi, Y.; Wang, Z.; Wang, Y.; Li, S.; Jia, X.; Hu, S. Terrestrial heat flow and crustal thermal structure of the Gonghe-Guide area, northeastern Qinghai-Tibetan plateau. *Geothermics* **2018**, *72*, 182–192. [CrossRef]
72. Liu, Q.Y.; van der Hilst, R.D.; Li, Y.; Yao, H.J.; Chen, J.H.; Guo, B.; Qi, S.H.; Wang, J.; Huang, H.; Li, S.C. Eastward expansion of the Tibetan Plateau by crustal flow and strain partitioning across faults. *Nat. Geosci.* **2014**, *7*, 361–365. [CrossRef]
73. Huang, X.; Xu, X.; Gao, R.; Guo, X.; Li, W. Shortening of lower crust beneath the NE Tibetan Plateau. *J. Asian Earth Sci.* **2020**, *198*, 104313. [CrossRef]